A PASSIVE MILLIMETER-WAVE IMAGER USED FOR CONCEALED WEAPON DETECTION

Cheng Zheng*, Xianxun Yao, Anyong Hu, and Jungang Miao

School of Electronic and Information Engineering, Beihang University, Xueyuan Road 37th, Haidian District, Beijing 100191, China

Abstract—An 8 mm-band passive millimeter-wave imager BHU-2D has been developed by Beihang University. This imager is designed for detecting concealed weapons on human body. The imager adopts two-dimensional synthetic aperture interferometric radiometer (SAIR) technique which avoids the radiation risk to human body. Compared with scanning technique, SAIR technique could obtain images of a larger field of view (FOV) while achieving high imaging rate, which are necessary for security monitoring. In this paper, the imaging principle of SAIR is stated firstly. Secondly, background cancellation method designed for BHU-2D is interpreted. The technique is used to reduce the complexity as well as the dimensional requirements of the receiving elements. Thirdly, system configuration is illustrated in detail. Then external point source calibration method is introduced and discussed specifically for security check applications. Finally, imaging experiments on a person with concealed weapon are conducted by which the design and image calibration algorithms are verified. To conclude, experimental results prove that BHU-2D could be employed in security check applications.

1. INTRODUCTION

The detection of concealed weapon on human body is an increasingly important topic in the security check practice. Individuals carrying weapons into airplanes, schools, and some other establishments are threats to the public security. In order to eliminate those threats, sensors like metal detectors are widely used to detect the prohibit items at present. However, it is not sufficient because the sensors cannot

detect weapons made up of non-metal materials, such as ceramic, plastic, etc.

Currently, much attention has been attracted on systems employing passive millimeter-wave imaging technique since it could detect non-metal weapons through textile material [1–21]. With adequate aperture size, imagers operating at millimeter-wave frequency can achieve a sufficient resolution to detect the position and geometry of the concealed objects. Unlike X-ray machines or radar instruments, passive imagers do not emit electromagnetic energy. They receive the spontaneous radiation emitted or reflected by the subject of interest. Therefore, passive millimeter-wave imagers are safe for the human body.

A two-dimensional passive millimeter-wave imager BHU-2D used for concealed weapon detection has been developed in Beihang University. Since security applications usually require high imaging rate and large FOV, antenna array technique is preferred for BHU-2D.

The typical passive millimeter-wave imaging systems for portal security screening nowadays are based on focal plane array (FPA) and phased array (PA) technique [1, 2]. FPA systems consist of a quasi-optical subsystem and a receiver/detector array. The output of one receiver gives one pixel in the image of the FOV. In order to obtain better spatial resolution, the receiver/detector array requires many channels, hundreds to perhaps a thousand. For the purpose of reducing the number of the channels, a mechanical scanning subsystem is usually employed [3–5], which slows down the imaging rate. Besides, the scanning subsystem may require daily maintenance more frequently. Another problem of FPA systems is that they have insufficient depth-of-field, which is not suitable for security monitoring [6]. PA systems consist of an antenna/receiver array, a group of phase sorters and a detector [7]. PA systems scan the FOV electronically, therefore they could achieve higher imaging rate. Since the amplifiers of PA systems are moved to the pupil plane, each individual amplifier contributes to the entire image rather than to an individual pixel. Consequently, PA systems could obtain the image of the FOV with a sparse antenna array and achieve much longer mean time between failures (MTBF) [6, 8]. The problem of the PA systems is that they could only obtain the images pixel by pixel. In order to reduce the time to take a whole image, the integration time corresponds to one pixel is short. For the purpose of increasing the signal-to-noise ratio (SNR) with short integration time, more receiving channels are usually used. Furthermore, the abilities to match electrical path lengths and adjust the phase sorters among hundreds of broadband receivers are challenges actually [8].

SAIR systems consist of an antenna/receiver array and a cross-correlator array. Compared with FPA systems, the antennas/receivers in the SAIR systems work in the pupil plane, which allows employing a sparse antenna array and achieving longer MTBF. Compared with PA systems, SAIR systems obtain all the pixels of the image in one shot and all the pixels share a longer integration time than PA systems. Consequently, there would be fewer receivers in the SAIR systems than PA systems. Furthermore, the density of the receiver array in SAIR system is lower than PA system, too. Although the signal processing subsystem of SAIR system is more complicated than FPA and PA system, the development of digital circuits at present is capable of meeting the requirements of SAIR systems with reasonable volume, cost and power consumption [9]. In order to achieve high imaging rate with lower cost and lower complexity of the receiving array, SAIR technique is applied to BHU-2D.

BHU-2D consists of an antenna array with 24 receiving elements and a digital signal processing subsystem. The 24 receiving elements are installed on a plane in Y-shaped geometry. The digital signal processing subsystem is used to calculate the visibility function samples and reconstruct the millimeter-wave image in real-time. For the purpose of reducing the complexity of the system, background cancellation and external point source calibration are designed and implemented in BHU-2D. The design, configuration, calibration method and some experiment results of BHU-2D are presented in this paper.

2. SYSTEM DESIGN

2.1. General Imaging Principle

The principle of SAIR is to measure the spectral components of the brightness temperature distribution in the FOV by correlating signals that are received by the antennas arranged in a plane. The correlation between the signals received by a pair of antennas is

$$V_{ij}(u,v) = \frac{1}{2}\mathrm{E}\left[s_i(t)\,s_j^*(t)\right] \tag{1}$$

where $V_{ij}(u,v)$ called visibility is the spatial frequency component, $s_i(t)$ and $s_j(t)$ are the signals received by the two antennas, and (u,v) is the vector between the two antennas in wavelength, which is usually called baseline. Based on Van-Cittert-Zernike Theorem [22], the relationship between visibility and brightness temperature in the

FOV is

$$V_{ij}(u, v) = \iint_{\xi^2+\eta^2\leq 1} T_M(\xi, \eta)\, \widetilde{r}_{ij}(-\tau)\, e^{-j2\pi(u\xi+v\eta)} d\xi d\eta \qquad (2)$$

where $T_M(\xi, \eta)$ is modified brightness temperature, $\widetilde{r}_{ij}(-\tau)$ the fringe washing function (FWF), and $\xi = \sin(\theta)\cos(\phi)$ and $\eta = \sin(\theta)\sin(\phi)$ are the direction cosines in spherical coordinate system. The modified brightness temperature could be expressed as

$$T_M(\xi, \eta) = \frac{T_B(\xi, \eta)}{\sqrt{1 - \xi^2 - \eta^2}} F_i(\xi, \eta) F_j^*(\xi, \eta) \qquad (3)$$

where $T_B(\xi, \eta)$ is the brightness temperature, $F_i(\xi, \eta)$, and $F_j(\xi, \eta)$ are the antenna patterns of the two antennas. Finally, the FWF could be calculated by the following equation

$$r_{ij}(\tau) = \int_0^\infty H_{ni}(f)\, H_{nj}^*(f)\, e^{j2\pi f\tau} df \qquad (4)$$

where $H_{ni}(f)$ and $H_{nj}(f)$ are the normalized frequency responses of the two receivers, and $\tau = -(u\xi + v\eta)/f_0$, where f_0 is the center frequency of the receivers. Equation (2) shows that $T_B(\xi, \eta)$ could be reconstructed by calculating the inverse Fourier transform (IFT) of the visibilities.

2.2. Background Cancellation Technique

Equation (2) is an integral form of the imaging principle. Practically, each pair of the antennas in the array composes a baseline and the visibility function $V(u, v)$ corresponding to the baseline can be measured. Consequently, the visibility function is sampled by the antenna array. When the sampling spacing does not meet the Nyquist Theorem, aliasing error will be introduced in the SAIR system. Assume the FOV of an SAIR is a unit circle, as shown in Fig. 1(a). The overlap situation in hexagonal sampling [23] condition is shown in Fig. 1(b). The anti-aliasing FOV could be expressed as

$$\theta_{\max} = 2\arcsin\left(\frac{2}{\sqrt{3}d} - 1\right) \qquad (5)$$

where d is the spacing between visibility function samples. Consequently, $d < 2\lambda/\sqrt{3}$ is required in hexagonal sampling condition to preserve an anti-aliasing FOV, where λ is the wavelength corresponding to the center frequency of the receiver. However, the angular resolution in this condition could be expressed as [24]

$$\Delta\xi \approx \frac{\pi\lambda}{4\rho_{\max}} \qquad (6)$$

where $\rho_{\max} = Nd/\sqrt{3}$ is the largest baseline, and N is the number of the antennas. Equation (6) shows that the angular resolution is determined by the coverage of the visibility function samples, while Equation (5) shows that the anti-aliasing FOV is determined by the grid spacing among the visibility function samples. When large FOV and high resolution is required, the sampling spacing d is a tradeoff between Equations (5) and (6) for a given N. In order to reduce the requirements of sampling spacing, background cancellation technique is designed for BHU-2D.

Background cancellation is a method to reduce the influence of the aliasing error caused by under sampling of the visibility function. As shown in Fig. 1(a), the unit circle could be divided into imaging region and background region based on the overlapping condition. As could be seen in Figs. 1(b) and (c), the unit circle is overlapped in the recovered image while the imaging region does not overlap with itself. Then, visibility function samples of the FOV could be measured with and without the target respectively and then the visibility function sample could be calculated by

$$V_{T-B_0}(u,v) = V_{T+B}(u,v) - V_{B_0+B}(u,v)$$
$$= \iint_{(\xi,\eta)\in\mathrm{IR}} \left[T_M^T(\xi,\eta) - T_M^{B_0}(\xi,\eta) \right] \widetilde{r}_{ij}(-\tau) e^{-j2\pi(u\xi+v\eta)} d\xi d\eta \quad (7)$$

where $V_{B_0+B}(u,v)$ is the visibility function sample without the target, $V_{T+B}(u,v)$ the visibility function sample with the target, IR the imaging region, and $T_M^T(\xi,\eta)$ and $T_M^{B_0}(\xi,\eta)$ are the brightness temperature with and without the target. Equation (7) shows that $V_{T-B_0}(u,v)$ does not contain the information of the background region. Since imaging region does not overlap with itself, image reconstruction on $V_{T-B_0}(u,v)$ is free from aliasing error. Therefore image reconstructed with $V_{T-B_0}(u,v)$ expresses the brightness distribution
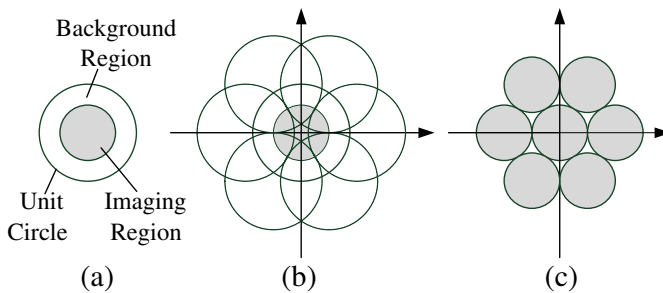

Background
Region

Unit   Imaging
Circle   Region

(a)   (b)   (c)

Figure 1. Background cancellation technique.

of the target, but with a difference of the background brightness temperature $T_{B_0}(\xi, \eta)$. Consequently, image reconstruction on $V_{T-B_0}(u, v)$ requires $T_{B_0}(\xi, \eta)$ to be uniform in imaging region. For a given d in hexagonal sampling condition, the anti-aliasing FOV with background cancellation technique is expressed as

$$\theta_{\max}^{\mathrm{BC}} = 2\arcsin\left(\frac{1}{\sqrt{3}d}\right) \tag{8}$$

With background cancellation method, the requirement of d is reduced. For a requested angular resolution and FOV, the antenna array could be achieved with fewer receiving elements, which reduces the complexity and cost of the system.

2.3. Antenna Array of BHU-2D

Based on background cancellation technique, the antenna array of BHU-2D is designed. There are 24 receiving elements in BHU-2D and they are installed on a plane in Y-shaped geometry. The Y-shaped configuration is adopted because it generates less redundant visibility function samples than T- or U-shaped array, therefore it could make full use of the 24 elements. Furthermore, hexagonal sampling of visibility function achieves larger anti-aliasing FOV than rectangular sampling with the same element spacing [23]. In order to enlarge the FOV and reduce the dimension requirements of the receiving element, the hexagonal sampling is employed.

Figure 2 shows the configuration of the array. There are three arms in the array and 8 receiving elements per arm. The spacing
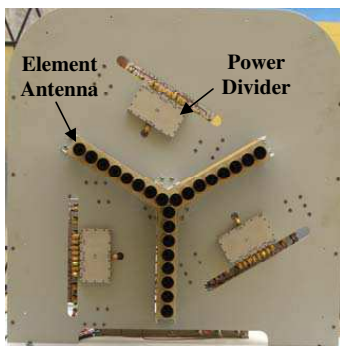
Figure 2. Antenna array of BHU-2D.
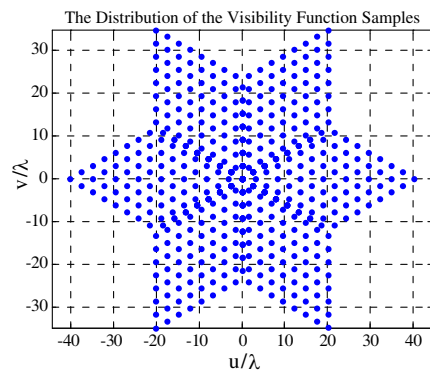
Figure 3. Distribution of visibility function samples.

between elements is 27 mm, i.e., 3.07λ. The distribution of the visibility function samples are illustrated in Fig. 3. There are 427 unique baselines in the system. The spacing between visibility function samples is 3.07λ and the anti-aliasing FOV is about 20 degrees with background cancellation technique. As shown in Fig. 3, the largest baseline of the instrument is 40.3λ and the angular resolution is 1.1 degrees.

3. INSTRUMENT DESCRIPTION

3.1. System Configuration

A simplified block diagram of BHU-2D is illustrated in Fig. 4 and the main specifications are listed in Table 1. The instrument consists of 24 8 mm-band receiving elements located in a Y-shaped geometry. Each element is composed of a Potter horn and a dual-conversion receiver with I/Q demodulator. Coherent LOs are generated by a frequency synthesizer and fed into receivers through a group of dividers. A Digital Signal Processing (DSP) subsystem computes complex cross-correlations between the IF output signals of all receivers simultaneously. The cross-correlations will be calibrated to form visibility function samples. By calculating the IFT of the visibility function samples, a brightness temperature image of the FOV could be obtained.
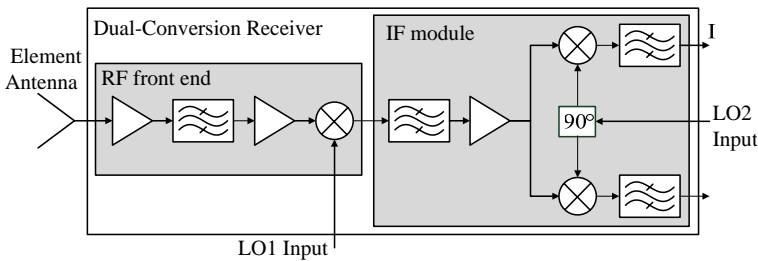
3.2. Receiving Elements

Every receiving element in the antenna array is composed of an element antenna and a dual-conversion receiver. Fig. 5 shows the block diagram of the receiving element.
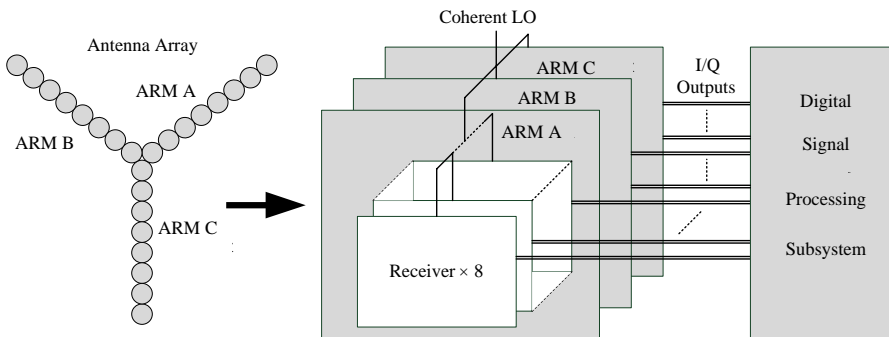
**Figure 4.** System configuration of BHU-2D.

Table 1. The main specifications of the BHU-2D.

Parameter	Specification
Center Frequency	34.1 GHz
Bandwidth	160 MHz
LO Frequency	32 GHz (used for RF front end)
	2 GHz (used for I/Q demodulator)
Field of View	20°
Synthetic Beamwidth	1.1° (Rectangle window)
	1.5° (Hanning window)
Temperature Sensitivity	~ 1 K (0.5 s integration time)
	~ 3 K (0.05 s integration time)
Geometry of Antenna Array	Y-shaped
Number of Receiving Elements	24
Antenna Element Spacing	27 mm (3.07 wavelengths)
Number of Baselines	427
Number of Correlators	924
Number of Cross Correlators	852
Calibration	Noise Injection (External Point Source)
	Background Cancellation

Figure 5. Block diagram of the receiving element.

As is shown in Equation (3), modified brightness temperature is proportional to the antenna pattern of the element antenna, which means antenna pattern should be measured precisely before image reconstruction. However, this is sometimes impractical when the element antenna is embedded in an array due to the mutual coupling among neighboring elements and imperfections of manufacture. Consequently, low mutual coupling antennas will be desirable. Parabolic Potter horn is adopted for its low coupling character. The outer diameter of the horn is 27 mm, which can make
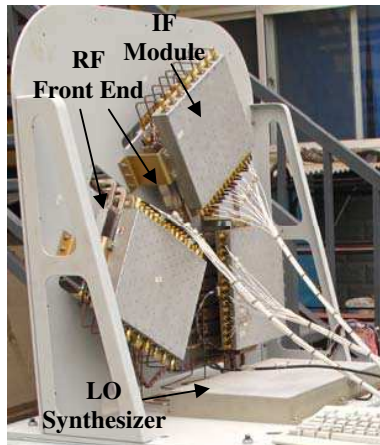
Figure 6. Configuration of the receiver array.

full use of the spacing between antennas and maximize the main beam efficiency. The -3 dB beam width of the element antenna is about 20 degrees, which is consistent with the FOV.

The signals collected by the antennas are fed into a group of dual-conversion receivers with I/Q demodulators. As is shown in Fig. 5, each receiver consists of a RF front end and an IF module. The RF front end converts the radio frequency signal into lower frequency signal, which will be then demodulated into I/Q outputs by the IF module. Both down-converters in the RF front end and the IF module operate in single sideband mode. The nominal gain and noise temperature of the receivers are 100 dB and 370 K respectively. In order to equalize the gain between channels, the gain of each IF module can be adjusted by a variable attenuator. Fig. 6 shows the configuration of the receiver array. For the purpose of reducing the dimension of the instrument, the receivers are installed parallel to the array. The RF front end and the IF module are installed in two layers, as is shown in Fig. 6.

3.3. Digital Signal Processing Subsystem

The I/Q outputs of the receivers are digitized and the complex correlations between signals are calculated in the DSP subsystem. Considering the bandwidth of the complex IF signal is about 160 MHz, the sampling rate is set to 200 MSPS based on the Nyquist theory, which means about 1000 correlators should operate at 200 MHz. To achieve such a high processing rate with a reasonable complexity and power consumption, 1 bit/2 level digital correlators [25] are used and implemented in a FPGA. For 1 bit/2 level correlator only gives the

correlation coefficient of the input signals, the power of the input
signals are required to denormalize the coefficients into visibility
function samples.

The block diagram of the DSP subsystem is illustrated in Fig. 7.
There are 48 data acquisition elements in the DSP. The quantization
resolution is 8 bits to meet the requirements of power measurement
units. After power measurement, the 8-bit data are converted into
1-bit data by comparators. In order to calibrate the offset errors of
the ADCs, the average of the signals are estimated and set as the
thresholds of the comparators. After receiving the 1-bit data, the
correlator unit computes the correlation coefficients with the 1-bit
data. There are 852 cross-correlators (4 correlators per baseline) in
the unit. Besides, 72 additional correlations are calculated, including
24 correlations between I/Q outputs of one receiver as well as 48
correlations between the sign bit data and artificial vectors of "all
ones" (probability estimation). The former is used to calibrate the
quadrature error, while the latter is required to calibrate the threshold
errors of the comparators [26]. Finally, the correlation coefficients and
the power measurements are collected, and then the visibility function
samples could be calculated by the computer. By calculating the IFT
of the visibility function samples, a brightness temperature image could
be obtained in the computer. Fig. 8 shows the structure of the DSP
subsystem. Every Data Acquisition Unit (DAU) consists of 16 data
acquisition elements. The 1-bit data is transmitted to Correlation
Array Unit (CAU) by Rocket IO lanes and the correlation coefficients
are calculated in CAU. The SYNC unit is designed to synchronize CAU
and DAUs. The DSP subsystem is installed in a standard 6U platform.
An external view of the deployed instrument is shown in Fig. 9.
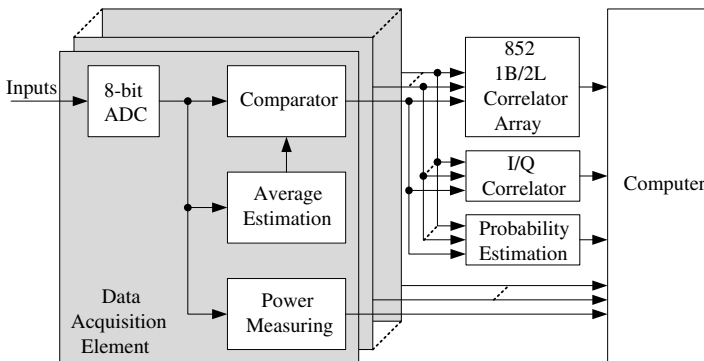
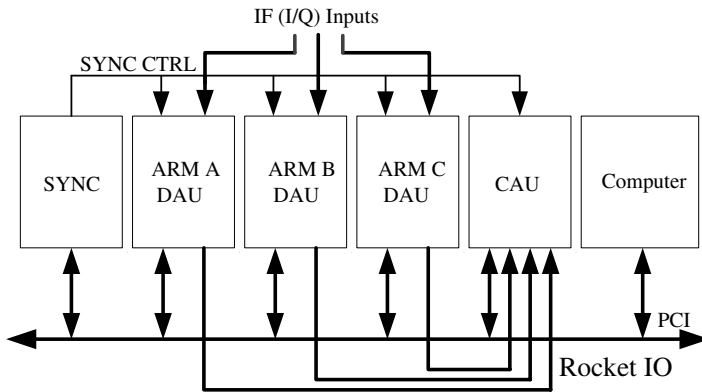**Figure 7.** Block diagram of the DSP subsystem.

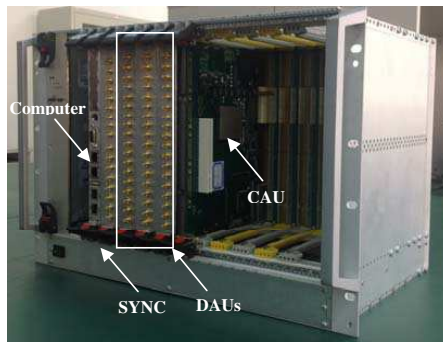**Figure 8.** The structure of the DSP subsystem.

Figure 9. DSP subsystem of the BHU-2D.

3.4. Calibration

Considering the imperfections of the manufacture and the drift of the receivers, there will be some slight differences among the receiving elements. In order to calibrate the errors introduced by the differences, noise injection method is used.

For the purpose of reducing the complexity of the system, the noise distribution network for noise injection calibration is replaced with an external point noise source in BHU-2D. It is located in the center of the FOV. The visibility function samples of the point source are measured before actual imaging. When the noise source is an ideal point source,

the calibrated visibility function samples could be expressed as

$$
\begin{aligned}
V_{\text{norm}}(u, v) &= V_T(u, v) / V_P(u, v) \\
&= \frac{\iint_{\xi^2 + \eta^2 \leq 1} T_M^T(\xi, \eta) \, \widetilde{r}_{ij}(-\tau) \, e^{-j2\pi(u\xi + v\eta)} d\xi d\eta}{\iint_{\xi^2 + \eta^2 \leq 1} T_M^P(\xi, \eta) \, \widetilde{r}_{ij}(-\tau) \, e^{-j2\pi(u\xi + v\eta)} d\xi d\eta} \\
&= \iint_{\xi^2 + \eta^2 \leq 1} \frac{T_M^T(\xi, \eta) \, \widetilde{r}_{ij}(-\tau)}{T_M^P(0, 0) \, \widetilde{r}_{ij}(0)} e^{-j2\pi(u\xi + v\eta)} d\xi d\eta \quad (9)
\end{aligned}
$$

where V_T and V_P are the visibility function samples of the target and the noise source respectively. When the target and noise source are in the far field of the instrument, the difference between $\widetilde{r}_{ij}(-\tau)$ and $\widetilde{r}_{ij}(0)$ could be negligible. The error caused by the differences between receiving elements can be calibrated by Equation (9). If the target or the noise source is not far enough from the instrument, the difference between $\widetilde{r}_{ij}(-\tau)$ and $\widetilde{r}_{ij}(0)$ cannot be negligible, especially the phase of the FWF [27]. In this situation, the target and the noise source should be located in the same position in order to reduce the phase error.

In order to calibrate the aliasing error on visibility function samples and make the noise source an ideal point source, Equation (9) could be converted into

$$
V_{\text{norm}}(u, v) = \frac{V_{T+B}(u, v) - V_{B_0 + B}(u, v)}{V_{P+B}(u, v) - V_{B_0 + B}(u, v)} \quad (10)
$$
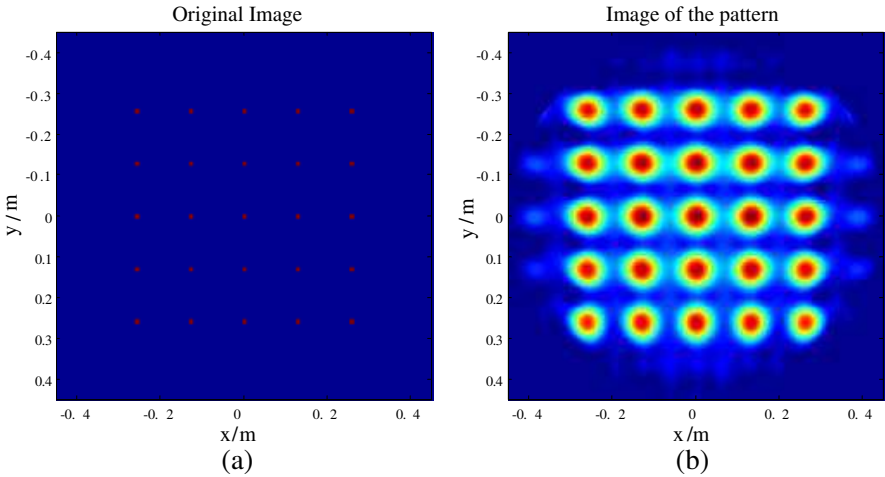
Figure 10. Simulation of a pattern consists of several point sources. (a) Original image. (b) Image of the pattern.

Considering $V_{B_0+B}(u, v)$ and $V_{P+B}(u, v)$ could be measured with longer integration time, the temperature resolution is determined by $V_{T+B}(u, v)$ and will not get worse. By calculating the IFT of the visibility function samples $V_{\mathrm{norm}}(u, v)$, a brightness temperature image of the imaging region could be reconstructed.

A simulation is carried out to estimate the error caused by the calibration method. In the simulation, the distance between the target and the instrument is 2.5 m. Fig. 10 shows the simulation result. From Fig. 10(b), the amplitude error and position error of the points could be concluded: The amplitude error is less than 0.6 dB and the position error is less than 6 mm.

4. EXPERIMENTAL RESULTS

For the purpose of validating the design and the calibration method, imaging experiments on a point source and a person are conducted.

4.1. Imaging Results of a Point Source

The point source is located in front of the instrument and the distance between them is 2.5 m. As is discussed above, the target should be at the same position as the calibration source because it is within the near field region. Since the solid angle subtended by the point source is smaller than the imaging resolution, the image of the point source
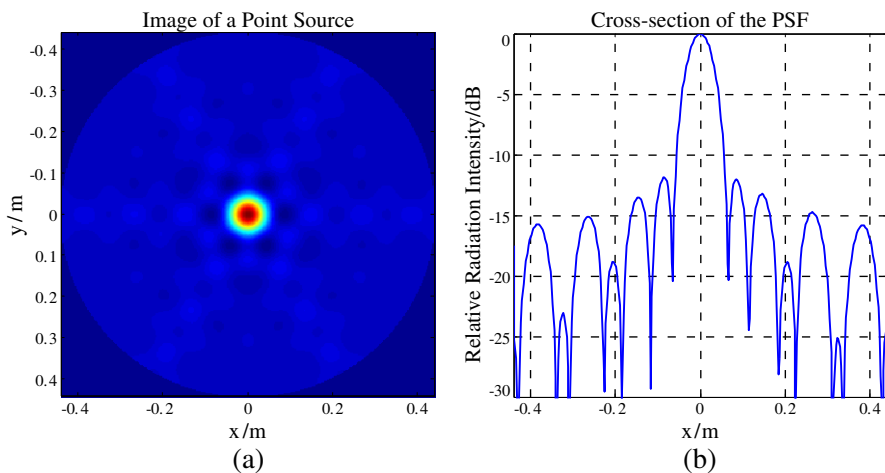
Figure 11. PSF of BHU-2D. (a) PSF of BHU-2D. (b) Cross-section $(y = 0)$ of the PSF.
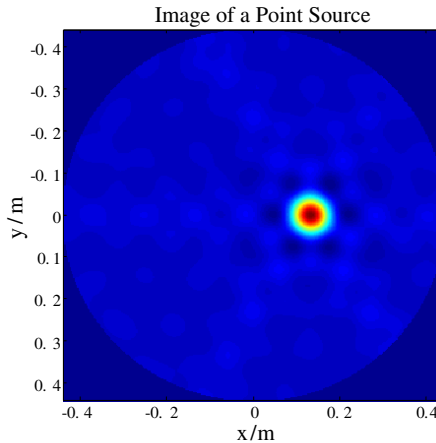
**Figure 12.** Imaging result of a shifted point source.

can be interpreted as the point spread function (PSF) of the system. Fig. 11(a) shows the result. In order to reduce the influence of the side lobe, Hanning window is applied before image reconstruction. The hexagonal side lobe caused by the limited spatial frequency coverage can be seen clearly in the figure. Fig. 11(b) shows the cross-section of the PSF, from which it could be seen that the angular resolution is about 1.5 degrees [24, 28], which is coincident with the design specification. Fig. 12 shows the imaging result of a point source located 13 cm to the right of the calibration source. As can be seen from the image, the point is in the position of 13.03 cm, which is coincident with its real position.

4.2. Imaging Results of a Person

Imaging experiment on a person is carried out. In order to form a uniform background, a metal plane with 45° incline to the ground is fixed behind the person. The plane can reflect the spontaneous radiation from the sky and form a uniform cold background. The integration time in the experiment is set to 0.5 s. The result is shown in Fig. 13. The pictures shown on the left in Fig. 13 is captured by a camera and the corresponding imaging results are on the right. Fig. 13(a) shows the image obtained by BHU-2D match that of the camera very well. In Fig. 13(b), the person is sitting behind a blanket and the blanket is completely transparent to BHU-2D, which is a useful property for concealed weapon detection. Fig. 13(c) shows a person with a knife concealed in his overcoat and the knife can be clearly recognized from millimeter-wave image.
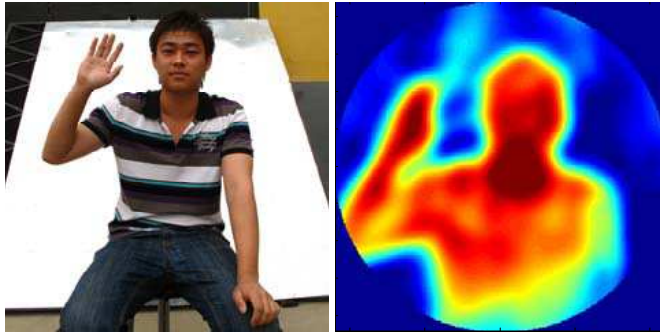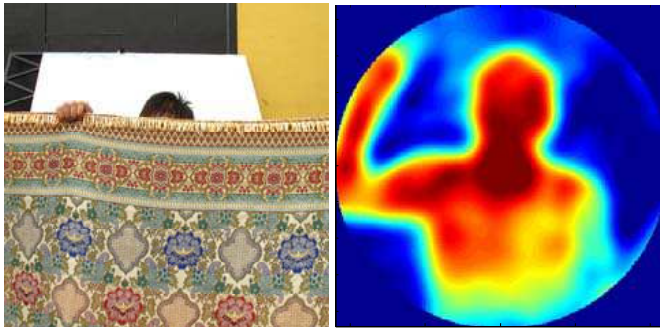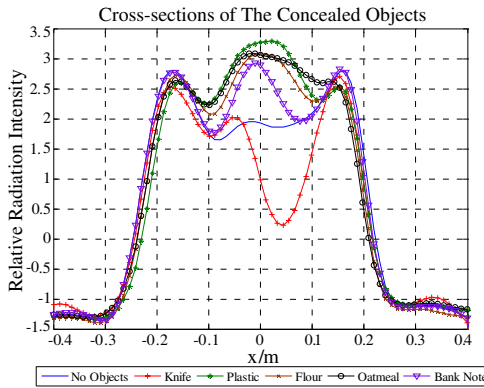
Figure 13. Imaging results of a person. (a) Imaging result of a person. (b) Imaging result of a person behind a blanket. (c) Imaging result of a person with concealed weapon.

Figure 14. Cross-sections of the images of a person with different concealed objects.

Further imaging experiments on a person with different concealed objects on his body are conducted in order to validate the capability of detecting concealed objects made up of non-metal materials. The setup of the experiment is the same as Fig. 13. An object is concealed in the person's overcoat. In the millimeter-wave image, the position corresponding to the objects is about $(0\,\mathrm{cm}, 16\,\mathrm{cm})$. When the millimeter-wave images are acquired, the cross-sections $(y = 16\,\mathrm{cm})$ of the images are plotted in Fig. 14. As could be seen, the concealed objects are positioned between $x = -0.1$ and $x = 0.1$. It also shows that the objects made up of plastic, powder, paper and metal could be distinguished from no concealed objects by BHU-2D.

5. CONCLUSION AND FUTURE WORK

A two-dimensional passive millimeter-wave imager BHU-2D has been developed by Beihang University. In order to reduce the complexity of the instrument, background cancellation and external point source method are designed and applied to BHU-2D. Imaging experiments show that BHU-2D is capable of detecting concealed weapons, which proves the design and calibration method. However, distortions caused by near-field imaging are not eliminated clearly. In order to decrease the near-field distortions, numerical image reconstruction algorithms are being developed. Our future efforts will focus on improving the FOV, spatial resolution and temperature resolution. In order to do so, an improved imager with more receiving elements and optimized antenna array is being developed. Also the approaches to improve the

temperature resolution, such as increasing receiving bandwidth and visibility function sample redundancy, are being studied.

REFERENCES

1. Goldsmith, P. F., C. T. Hsieh, G. R. Huguenin, J. Kapitzky, and E. L. Moore, "Focal plane imaging systems for millimeter wavelengths," *IEEE Trans. Microw. Theory Tech.*, Vol. 41, No. 10, 1664–1675, Oct. 1993.

2. Martin, C. A., S. E. Clark, J. A. Lovberg, and V. G. Kolinko, "Passive millimeter-wave imaging technology for phased array systems," *Proc. SPIE*, Vol. 5077, 33–41, Aug. 20, 2003.

3. Williams, T. D. and N. M. Vaidya, "A compact, low-cost, passive MMW security scanner," *Proc. SPIE*, Vol. 5789, 109–116, May 19, 2005.

4. Notel, D., J. Huck, S. Neubert, S. Wirtz, and A. Tessmann, "A compact MMW imaging radiometer for concealed weapon detection," *Proc. IRMMW-THz*, 269–270, Cardiff, Sep. 2–9, 2007.

5. Kim, W., N. Moon, Y. Chang, M. Lee, S. Jung, J. Choi, J. Jung, and Y. Kim, "System design of focal plane array based millimeter-wave imaging radiometer for concealed weapon detection," *Proc. IGARSS*, 2258–2261, Vancouver, BC, Jul. 24–29, 2011.

6. Salmon, N. A., J. Beale, and S. Hayward, "Compact and lightweight digital beam-forming passive millimeter imagers," *Proc. SPIE*, Vol. 7117, 711709, Oct. 2, 2008.

7. Kolinko, V. G., S. Lin, A. Shek, W. Manning, C. Martin, M. Hall, O. Kirsten, J. Moore, and D. A. Wikner, "A passive millimeter-wave imaging system for concealed weapons and explosives detection," *Proc. SPIE*, Vol. 5781, 85–92, May 19, 2005.

8. Lovberg, J. A., C. Martin, and V. G. Kolinko, "Video-rate passive millimeter-wave imaging using phased arrays," *Proc. MWSYM*, 1689–1692, Honolulu, HI, Jun. 3–8, 2007.

9. Salmon, N. A., P. N. Wilkinson, C. T. Taylor, and M. Benyezzar, "Minimising the costs of next generation aperture synthesis passive millimetre wave imagers," *Proc. SPIE*, Vol. 8188, 818808, Oct. 6, 2011.

10. Salmon, N. A., J. Beale, A. Beard, M. Dean, S. Hayward, P. Hickling, S. T. Chiw, H. Ghafouri-Shiraz, P. Hall, R. Macpherson, R. Lewis, A. H. Lettington, and D. Dunn, "An all electronic passive millimetre wave imaging system," *Proc. SPIE*, Vol. 5789, 11–15, May 19, 2005.

11. Salmon, N. A., R. Macpherson, A. Harvey, P. Hall, S. Hayward, P. Wilkinson, and C. Taylor, "First video rate imagery from a 32-channel 22-GHz aperture synthesis passive millimetre wave imager," *Proc. SPIE*, Vol. 8188, 818805, Oct. 6, 2011.

12. Macfarlane, D. G., J. C. G. Lesurf, and D. A. Robertson, "Close range millimetre wave imaging," *Proc. SPIE*, Vol. 4719, 350–358, Jul. 25, 2002.

13. Martin, C. A. and V. G. Kolinko, "Concealed weapons detection with an improved passive millimeter-wave imager," *Proc. SPIE*, Vol. 5410, 252–259, Aug. 12, 2004.

14. Doghri, A., A. Ghiotto, T. Djerafi, and K. Wu, "Early demonstration of a passive millimeter-wave imaging system using substrate integrated waveguide technology," *Proc. MMS*, 215–218, Hammamet, Sep. 8–10, 2011.

15. Huang, J. and T. Gan, "A novel millimeter wave synthetic aperture radiometer passive imaging system," *Proc. ICMMT*, 414–417, Aug. 18–21, 2004.

16. Yeom, S., D. Lee, J. Son, and S. Kim, "Concealed object detection using passive millimeter wave imaging," *Proc. ICUS*, 383–386, Beijing, China, Oct. 18–19, 2010.

17. Yeom, S., D. Lee, J. Son, M. Jung, Y. Jang, S. Jung, and S. Lee, "Concealed object detection with radiometric imaging," *Proc. APSAR*, 1–4, Seoul, Sep. 26–30, 2011.

18. Lee, H., D. Lee, S. Yeom, J. Son, V. P. Guschin and S. Kim, "Passive millimeter wave imaging and analysis for concealed object detection," *Proc. ICMiA*, 98–101, Macao, Oct. 24–26, 2011.

19. Essen, H., H.-H. Fuchs, D. Notel, F. Kloppel, P. Pergande, and S. Stanko, "Passive millimeter-wave imaging at short and medium range," *Proc. SPIE*, Vol. 5989, 598916, Oct. 13, 2005.

20. Jacobs, E. L. and O. Furxhi, "Performance modeling of a passive interferometric millimeter wave sensor," *Proc. SPIE*, Vol. 7309, 730905, May 1, 2009.

21. Wikner, D. A., "Progress in millimeter-wave imaging," *Proc. SPIE*, Vol. 7936, 79360D, Feb. 10, 2011.

22. Goodman, J. W., *Statistical Optics*, 207–221, Wiley Classics Library Edition, Wiley, New York, 2000.

23. Dudgeon, D. E. and R. M. Mersereau, *Multidimensional Digital Signal Processing*, Ch. 1, Prentice Hall, Upper Saddle River, NJ, 1984.

24. Camps, A., "Application of interferometric radiometry to earth observation," Ch. 3, Ph.D. Dissertation, Polytechnic University of

Catalonia, Spain, 1996.

25. Ruf, C. S., "Digital correlators for synthetic aperture interferometric radiometry," *IEEE Trans. Geosci. Remote Sens.*, Vol. 33, No. 5, 1222–1229, Sep. 1995.

26. Corbella, I., F. Torres, A. Camps, A. Colliander, M. Martín-Neira, S. Ribo, K. Rautiainen, N. Duffo, and M. Vall-llossera, "MIRAS end-to-end calibration: Application to SMOS L1 processor," *IEEE Trans. Geosci. Remote Sens.*, Vol. 43, No. 5, 1126–1134, May 2005.

27. Zhang, C., J. Wu, H. Liu, and W. Y. Sun, "Near field imaging of synthetic aperture radiometer," *PIERS Online*, Vol. 4, No. 8, 886–890, 2008.

28. Li, Y., J. W. Archer, J. Tello, G. Rosolen, F. Ceccato, S. G. Hay, A. Hellicar, and Y. J. Guo, "Performance evaluation of a passive millimeter-wave imager," *IEEE Trans. Microw. Theory Tech.*, Vol. 57, No. 10, 2391–2405, Oct. 2009.